Applied Physics B (2019) 125:63
https://doi.org/10.1007/s00340-019-7179-y

Applied Physics B
Lasers and Optics

RAPID COMMUNICATION

Optical measurements of temperature fields in sooting flames: influence of soot self-absorption

Qianlong Wang[1] · Guillaume Legros[2] · Céline Morin[3] · Mingfa Yao[1] · Weiwei Cai[4] · Liqiao Jiang[5]

Received: 13 November 2018 / Accepted: 22 March 2019 / Published online: 29 March 2019

Abstract

Regular pyrometry techniques have been extensively used to infer the temperature field in sooting flames from soot luminosity. However, correction for soot self-absorption along the line-of-sight needs to be considered. The original contribution of the present paper is to assess both numerical and experimental uncertainties that can be attributed to the soot self-absorption effect on the soot temperature field measured by the two-color Modulated Absorption/Emission (2C-MAE) technique. Unlike for regular pyrometry techniques, the design of the 2C-MAE technique actually enables the direct measurement of the local spectral absorption coefficient field. The proportion of flame emission trapping caused by the soot along the line-of-sight is first simulated for different levels of soot loading ranges. The retrieved temperature error when self-absorption is neglected can then be quantified as a function of the level of soot loading and the detection spectral ranges of the technique. As a result, it is found that the proportion of the flame emission attenuation due to self-absorption is directly proportional to the soot volume fraction f_v and hardly depends on the temperature field to be retrieved. These trends are emphasized as the lower spectral range of detection is shifted towards the smaller wavelength. In addition, a linear correlation between the absolute temperature error and the peak f_v in the flame can be extracted and confirmed by experimental results. Eventually, it is also found that selecting detection spectral ranges centered at 645 nm and 785 nm offer the minimum temperature deviation when soot self-absorption is neglected for any conditions of soot loading level within the three studied spectral combinations. This finding is especially relevant for the identification of the optimal operating conditions required by regular 2C-pyrometry for the sooting flames considered.

1 Introduction

In the last decades, models of soot particles formation and oxidation processes have been extensively developed [1–4]. Integrated to fine numerical simulations of flames, some deliver fair predictions of local soot temperature and concentrations [3, 5]. However, the accuracy of these models in terms of soot production is proven to be strongly connected to the field of local soot temperature [3], which does depend highly on the field of local soot concentration, especially due to radiative heat transfer that is attributed to soot within the flame [6, 7]. Among others, steady laminar axisymmetric coflow non-premixed flames have then been paid special attention as this kind of academic flames exhibits zones where fuel pyrolysis, soot inception, growth, and oxidation can be readily identified along the flame height [8]. As a result, this flame configuration has been widely documented with measured soot temperature and volume fields [9–12].

Various optical diagnostics allow the measurement of local soot temperature and concentration in laminar flames, such as the two-color laser-induced incandescence technique (LII) [13–15] or the spectrally resolved LII [16, 17], the spectrally resolved flame emission technique [18–20], and the Modulated Absorption/Emission (MAE) one [21–23].

✉ Qianlong Wang
wangqianlong@tju.edu.cn

[1] State Key Laboratory of Engines, Tianjin University, Tianjin 300072, China

[2] Centre National de la Recherche Scientifique, Sorbonne Université, UMR 7190, Institut Jean Le Rond d'Alembert, 75005 Paris, France

[3] LAMIH CNRS UMR 8201, UVHC, 59313 Valenciennes, France

[4] School of Mechanical Engineering, Shanghai Jiaotong University, Shanghai 200240, China

[5] Chinese Academy of Sciences, Guangzhou Institute of Energy Conversion, Guangzhou 510640, China

With the aforementioned LII related techniques, the radiative contribution to the thermal relaxation that follows the laser heating of the particles is captured and soot temperature can be measured when fitting either the ratio of emission rates collected within two different spectral ranges or the Planck function over the emission spectrum that has been resolved. The local soot volume fraction is then inferred from the emission intensity at the temperature measured. While the LII-related techniques are very popular today, issues about the invasive feature of the laser heating are still debated, especially highlighting the discrepancy between smaller and bigger particles, as the former ones potentially experience significant mass losses due to sublimation [24].

In the regular spectrally resolved flame emission methodology [19], the local soot temperature at a given radial location r and axial one z in the axisymmetric flame is retrieved from the slope of $\ln [E(m_\lambda)S_\lambda(r,z)^{-1}\lambda^{-6}]$ as a function of λ^{-1}, λ being the wavelength, $E(m_\lambda)$ a function of the complex refractive index of soot m_λ, and $S_\lambda(r,z)$ the local spectral emission rate. The above logarithmic expression can be derived provided a model connecting the local spectral absorption coefficient to the local soot volume fraction. Subsequently, the local soot volume fraction can be obtained, first inferring the local spectral absorption coefficient κ_λ attributed to soot, as $\kappa_\lambda = S_\lambda/B_\lambda(T)$ with $B_\lambda(T)$ the Planck's law at the measured temperature T, then using the aforementioned model to evaluate the soot volume fraction.

In contrast, the MAE technique requires an additional optical setup that allows collimated laser beams to probe the whole flame. Doing so, both laser attenuation and flame emission are imaged. As a result, the local spectral absorption coefficient fields κ_{λ_1} and κ_{λ_2} are measured within two different spectral ranges centered at λ_1 and λ_2. The local soot volume fraction field is then inferred also using a model of absorption coefficient. Concomitantly, the soot temperature is obtained from the ratio $B_{\lambda_1}/B_{\lambda_2}$ evaluated as $S_{\lambda_1}\kappa_{\lambda_2}/\kappa_{\lambda_1}S_{\lambda_2}$. Thus, the MAE methodology that yields the temperature measurement does not convey the uncertainty associated with the model of absorption coefficient [25]. Moreover, the signal processing underlying the MAE technique inherently includes the soot self-absorption along the line-of-sight. These features especially lead to a significantly low uncertainty in the temperature measurements inferred from flame emission, as identified by Michelsen [24, 27].

It is worth noticing that all the above-mentioned techniques are subject to soot self-absorption effect, also referred to as signal trapping. As an illustration, in the LII-related techniques, the soot volume fraction is deduced from the soot incandescence intensity, which is assumed proportional to the intensity captured by the camera sensor. Indeed, the incandescence intensity emitted by soot can be absorbed along the subsequent line-of-sight path to the sensor. Therefore, the self-absorption always reduces the signal magnitude reaching the sensor and causes the soot volume fraction underestimation. Consequently, this soot volume fraction underestimation would furthermore affect the temperature estimation accuracy. Some correction methods were developed for this LII signal attenuation [28–31]. Choi and Jensen [28] proposed a convergence criterion for the calibration factor to achieve the actual local soot volume fraction profiles within range of different degrees of sooting levels through iterative calculations. Furthermore, Liu et al. [29] and Daun et al. [30], respectively, calculated LII signal attenuation by solving the radiative transfer equation using the discrete-ordinates method and a backward Monte Carlo method. In their methods, the soot scattering is also accounted for, though it is verified that it is trivial to signal extinction in typical laminar diffusion flames at atmospheric pressure. Recently, Liu et al. [32] investigated the self-absorption influence on the retrieved soot temperature and volume fraction accuracy from spectrally resolved flame emission measurements. Two correction methods that were originally proposed by Freeman and Katz [26] and Snelling et al. [19] were employed to recover the unattenuated soot emission intensity. Because the former method is based on the linearization of exponential terms, it is expected to be accurate for small optical thicknesses. On the opposite, the latter method is not restricted to small optical thickness but is subject to the iteration error propagation and potential amplification. More recently, Nathan and Marshall [33] reported a self-absorption correction method in the color-ratio pyrometry, which is achieved by spatially resolved measurements of the soot absorption coefficient to correct the raw color-channel signal from soot via a color camera.

Though such studies on the self-absorption effect in LII, spectrally resolved flame emission measurements or color-ratio pyrometry can be found in the literature, none addresses the self-absorption effect in the MAE technique. Starting from the background related to the 2C-MAE technique [23], a parametric study first assesses here the importance of the self-absorption on the accuracy of the recovered soot temperature, as a function of soot loading level and detection spectral ranges. The absolute temperature error arising from the self-absorption within different soot loading levels is then quantitatively validated by experimental results.

2 Theoretical background

The basics of the 2C-MAE technique have been extensively detailed in Ref. [23]. However, the methodology reported in Sect. 3 will assess the limitations of both the 2C-MAE technique and any regular 2C-pyrometry. For this reason, the main features of the 2C-MAE technique and the associated procedure are described in this section especially to be contrasted with those of the 2C-pyrometry.

2.1 2C-MAE technique

The schematics illustrating the basics of the 2C-MAE technique are displayed in Fig. 1. In such a flame configuration, when the laser beam is blocked, the light-of-sight energy $\mathcal{E}_\lambda^0$ accumulated on a pixel during a time Δt due to the steady impinging flux emitted by the flame at wavelength λ can then be expressed as follows:

$$\mathcal{E}_\lambda^0 = \mathcal{E}_\lambda^{(\mathrm{off})} = \Delta\lambda\,\Delta t\,\Delta x^{\mathrm{pix}}\,\Delta z^{\mathrm{pix}}\,\eta_\lambda^{\mathrm{coll}}\,\Omega^{\mathrm{coll}} \int_{y_{\min}}^{y_{\max}} \kappa_\lambda(y)\,B_\lambda(y)\,e^{-\int_y^{y_{\max}} \kappa_\lambda(y')\mathrm{d}y'}\,\mathrm{d}y \tag{1}$$

where $\Delta\lambda$ is the detection wavelength bandwidth, Δx^{pix} and Δz^{pix} are the impinged pixel's dimensions, Ω^{coll} is the solid angle of collection, $\eta_\lambda^{\mathrm{coll}}$ is the overall efficiency of the collection optics, y is the coordinate along the optical pathway crossing the flame between $y_{\min}$ and $y_{\max}$, κ_λ is the local spectral absorption coefficient, and B_λ is the spectral blackbody radiative intensity at the local temperature, which could be calculated by the Planck's law:

$$B_\lambda = \frac{2\,h\,\pi\,c^2}{\lambda^5\left(e^{\frac{hc}{\lambda kT}}-1\right)} \tag{2}$$

When the laser is not blocked, the energy $\mathcal{E}_\lambda^{(\mathrm{on})}$ accumulated on the same pixel is $\mathcal{E}_\lambda^0$ complemented by the attenuated laser beam:

$$\mathcal{E}_\lambda^{(\mathrm{on})} = \mathcal{E}_\lambda^0 + \Delta t\,\Delta x^{\mathrm{pix}}\,\Delta z^{\mathrm{pix}}\,\eta_\lambda^{\mathrm{coll}}\,\phi_\lambda^{laser}\,e^{-\int_{y_{\min}}^{y_{\max}} \kappa_\lambda(y)\mathrm{d}y} \tag{3}$$

where $\phi_\lambda^{\mathrm{laser}}$ is the incoming laser flux. Thus, the absorption coefficient field $\kappa_\lambda(r,z)$ allows to be measured by consecutively $\mathcal{E}_\lambda^{(\mathrm{on})}$ and $\mathcal{E}_\lambda^{(\mathrm{off})}$ measurements:

$$\Delta t\,\Delta x^{\mathrm{pix}}\,\Delta z^{\mathrm{pix}}\,\eta_\lambda^{\mathrm{coll}}\,\phi_\lambda^{laser}\,e^{-\int_{y_{\min}}^{y_{\max}} \kappa_\lambda(y)\mathrm{d}y} = \mathcal{E}_\lambda^{(\mathrm{on})} - \mathcal{E}_\lambda^{(\mathrm{off})} \tag{4}$$

Because of the line-of-sight configuration, an onion-peeling method combined with a Tikhonov regularization is employed to deconvolution procedures to compute the local absorption coefficient fields. Thus, the discrete formulation inferred from Eq. (4) at a given height z_j above the burner, a linear system $2\mathbf{A}^{\mathrm{OP}}X = d$, is first to be solved for local absorption coefficient fields $X = \left(\kappa_{ij}\right)_{i=1,N}$. The $\mathbf{A}_{ik}^{\mathrm{OP}}$ elements are chord lengths that can be readily calculated using simple geometrical considerations:

$$A_{ik}^{\mathrm{OP}} = \begin{cases} 0 & \text{if } i > k \\ \Delta x^{\mathrm{pix}} * \left[k^2-(i-0.5)^2\right]^{0.5} & \text{if } i = k \\ \Delta x^{\mathrm{pix}} * \left(\left[k^2-(i-0.5)^2\right]^{0.5} - \left[(k-1)^2-(i-0.5)^2\right]^{0.5}\right) & \text{if } i < k \end{cases} \tag{5}$$

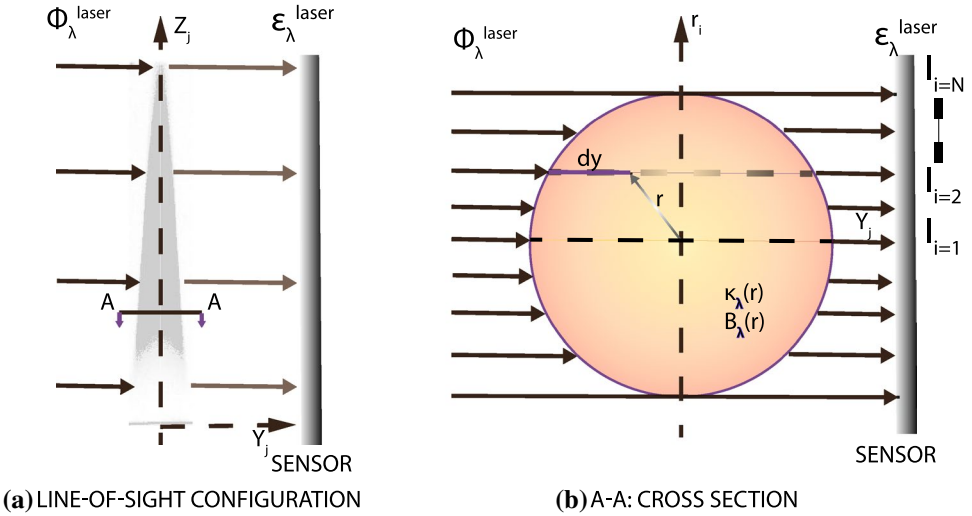

Fig. 1 Schematics of: **a** the axis-symmetric flame (shaded area) probed by a collimated laser beam (incoming energy $\phi_\lambda^{\mathrm{laser}}$; outcoming energy deposited on the sensor: $\mathcal{E}_\lambda^{\mathrm{laser}}$); **b** the line-of-sight to the sensor within a flame's cross section at a given height z_j above the burner. For legibility, the magnification ratio on the sensor is here set arbitrarily to unity and the optical arrangement enabling the telecentric configuration is not shown (see Ref. [23]). The sensor is represented by an entire row of pixels. $\left(I_{ij}\right)_{i=1,N}$ are the signals provided by the N pixels in this row

Assuming that soot particles are in the Rayleigh limit [35], the local soot volume fraction field $f_v(r,z)$ can also be inferred by Eq. (6):

$$f_v(r,z) = \frac{\lambda\,\kappa_\lambda(r,z)}{6\,\pi\,E(m)} \tag{6}$$

where $E(m_\lambda)$ is a function of the complex refractive index m_λ of soot. For the present study, the empirical law produced by Chang and Charalampopulos is selected [37], thus providing an evaluation of m as a function of wavelength.

When the $\kappa_\lambda(r,z)$ is given by the experiments, Eq. (1) can be solved for the local spectral emission rate $S_\lambda = \kappa_\lambda B_\lambda(r,z)$. Due to soot self-absorption along the line-of-sight, the contributions of the left and right quarters to any signal I_{ij} represented in Fig.1 are not identical. Therefore, some algebraic manipulations are needed to discrete Eq. (1). A general expression of the **C** elements is reminded as the following:

$$C_{ik} = \begin{cases} 0 & \text{if } k < i \\ A_{ik}^{\mathrm{OP}} e^{-\sum_{m=k+1}^{N} A_{im}^{\mathrm{OP}}\kappa_{mj}} (1 + e^{-A_{ik}^{\mathrm{OP}}\kappa_{kj}}) & \text{if } i = k < N \\ A_{ik}^{\mathrm{OP}} e^{-\sum_{m=k+1}^{N} A_{im}^{\mathrm{OP}}\kappa_{mj}} \left(1 + e^{-2\sum_{m=i}^{k-1} A_{im}^{\mathrm{OP}}\kappa_{mj} - A_{ik}^{\mathrm{OP}}\kappa_{kj}}\right) & \text{if } i < k < N \\ A_{ik}^{\mathrm{OP}} \left(1 + e^{-2\sum_{m=i}^{k-1} A_{im}^{\mathrm{OP}}\kappa_{mj} - A_{ik}^{\mathrm{OP}}\kappa_{kj}}\right) & \text{if } i < k = N \\ A_{ik}^{\mathrm{OP}} (1 + e^{-A_{ik}^{\mathrm{OP}}\kappa_{ik}}) & \text{if } i = k = N \end{cases} \tag{7}$$

Thus, the similar linear system $\mathbf{C}X = d$, which is discrete formulation inferred from Eq.(1), is then to be solved for local spectral emission rate $X = \left(\kappa_{ij}B_{ij}\right)_{i=1,N}$. Subsequently, the $B_\lambda(r,z)$ can then be extracted when computing the ratio $\kappa_\lambda B_\lambda/\kappa_\lambda$ for both λ_1 and λ_2. The soot temperature field of $T(r,z)$ can finally be inferred from a lookup table that provides T as a function of the ratio $B_{\lambda_2}/B_{\lambda_1}$.

It is worth highlighting that the interpretation of the soot spectral emission rate field expressed intrinsically includes soot self-absorption, as revealed by the exponential terms in the **C** matrix elements. In addition, the determination of the soot temperature by the 2C-MAE technique does not require any model for the spectral dependence of the soot refractive index as the fields of κ_λ are measured within both spectral ranges of detection.

2.2 2C-pyrometry technique

The methodology followed by any two-color pyrometry technique requires a specific processing to account for the soot self-absorption effect that can significantly affect the signals interpreted [21, 32, 36]. In the basic 2C-pyrometry technique, the self-absorption is usually neglected. Interestingly, when the exponential terms of the **C** matrix elements specified by Eq. (7) are forced to unity, **C** deteriorates to $\mathbf{A}^{\mathrm{OP}}$, and Eq. (1) turns to Eq. (8):

$$\mathcal{E}_\lambda^{0'} = \Delta\lambda\,\Delta t\,\Delta x^{\mathrm{pix}}\,\Delta z^{\mathrm{pix}}\,\eta_\lambda^{\mathrm{coll}}\,\Omega^{\mathrm{coll}} \int_{y_{\min}}^{y_{\max}} \kappa_\lambda(y)\,B_\lambda(y)\,\mathrm{d}y \tag{8}$$

In practice, the matrices of spectral intensity delivered in arbitrary unit (a.u.) by every pixel are processed, which provides with matrices of local spectral intensity I_λ^{loc}. Using Eq. (6), the ratio of local spectral intensities can be expressed as follows:

$$\frac{I_{\lambda_1}^{\mathrm{loc}}}{I_{\lambda_2}^{\mathrm{loc}}} = \alpha_{\mathrm{calib}}\frac{\kappa_{\lambda_1}B_{\lambda_1}}{\kappa_{\lambda_2}B_{\lambda_2}} = \alpha_{\mathrm{calib}}\frac{\lambda_2\,E(m_{\lambda_1})}{\lambda_1\,E(m_{\lambda_2})}\frac{B_{\lambda_1}}{B_{\lambda_2}} \tag{9}$$

where α_{calib} is a calibrating coefficient that can be set by the knowledge of the temperature at a location where the ratio of intensities is measured. In the present study, this is done at the peak local spectral intensity at λ_1, where the temperature is measured by the 2C-MAE technique. As $B_{\lambda_1}/B_{\lambda_2}$ is a monotonic function of T, the temperature T can then be obtained for any location (r, z), provided a model for the spectral dependence of m_λ. For a matter of consistency with the MAE procedure, the model assessed by Chang and Charalampopulos [37] is also used here.

The field of $B_\lambda(T)$ is then computed at either λ_1 or λ_2, which leads to the field of κ_λ as calculated by the ratio $\left(\kappa_\lambda B_\lambda\right)/B_\lambda$. Finally, Eq. (6) yields the fields of soot volume fraction f_v.

It is worth highlighting here that Eq. (9), which is the key step for the computation of the temperature field produced by the 2C-pyrometry, especially depends on a model for the spectral dependence of m_λ, together with a model connecting the soot volume fraction to the local spectral absorption coefficient. Both are shown to sustain ongoing debates in the combustion community [25].

3 Methodology

A systematic parametric study is first conducted to probe the significance of the soot self-absorption effect on the temperature measurements by 2C-MAE. An experimental assessment is then proposed in both 2C-MAE and 2C-pyrometry techniques.

3.1 Numerical parametric study

The temperature and soot volume fraction fields delivered by the numerical simulations conducted by Blacha et al. [12] were used by Legros et al. to assess the performances of the 2C-MAE technique [23]. The conditions are those of a standard Santoro flame, with a central ethylene flow rate of 0.231 L/min and a coflowing air flow rate of 43 L/min [38].

The soot volume fraction and the two detection spectral wavelengths (2C) selection are the two major factors that determine the self-absorption influence. To this end, the original soot loading level of Blacha et al. is increased by a factor of 2 and 5 to create medium and high soot loading, respectively, the temperature field being unchanged. Therefore, two groups of numerical studies are set up as follows:

* **Group 1**: three soot loading levels (peak f_v of approximately 10 ppm, 20 ppm, and 50 ppm)

* **Group 2**: three combinations of detection spectral ranges (645 nm & 485 nm, 645 nm & 532 nm, 645 nm & 785 nm)

It is noted that the soot temperature exists in Eq. (1), but it is irrelevant to the exponential term. Therefore, the soot temperature theoretically hardly affects the self-absorption. To testify this point, the medium and high temperature cases are also studied. Thus, the original soot temperature profiles of Blacha et al. are multiplied by a factor of 1.5 and 2, respectively. And the soot loading level remains unchanged. As a result, the relevant parametric results are shown in "Appendix A" to help the readers to straightforwardly understand this point.

For any given set of the above conditions, the temperature and soot volume fraction fields are interpolated onto a mesh grid whose cells have a characteristic width of 10 µm in both radial and axial directions. This length is very close to the spatial resolution of the projected data imaging the flame on the camera sensor used for the experimental study. The subsequent fields of soot temperature and volume fraction are then processed to build the fields of local spectral absorption coefficient $\kappa_\lambda(r,z)$ and local spectral emission rate $\kappa_\lambda B_\lambda(r,z)$, using Eqs. (6) and (2). As prescribed by Legros et al. [23], the synthetic frames can then be computed following Eqs. (1) and (3). Thus, the expected signals required as inputs of the deconvolution procedure are delivered.

It is worth emphasizing that these signal computations include the effect of soot self-absorption along the line-of-sight integration. Moreover, no noise is added to strictly identify the deviation when this effect is neglected along the deconvolution procedure. Finally, as the computation of $\kappa_\lambda(r,z)$ is unique here for both 2C-MAE and 2C-pyrometry techniques, the procedure of the latter technique only departs from that of the former one due to the omission of the soot self-absorption in the deconvolution processing.

3.2 Experimental assessment

The experimental database documenting our previous study [11] is used as a benchmark. The experimental parameters are specified in Table 1.

Table 1 Experimental parameters and main outputs of interest related to the investigations on the Santoro flame for different levels of O_2 dilution of the ethylene stream (extracted from Ref. [11])

Fuel flow			Coflow	Maximum f_v (ppm)	2C-MAE		2C-pyrometry	
C_2H_4 (l/min)	O_2 (l/min)	$X_{O_2}^{ax}$ (%)	Air (l/min)		AE (K)	SD (K)	AE (K)	SD (K)
0.231	0	0	43	9.7	53.0	132.8	294.4	550.2
	0.02	8		14.8	46.7	119.1	119.9	203.9
	0.04	14		17.8	51.6	113.2	124.2	266.4
	0.06	20		23.8	66.0	120.9	102.1	205.4
	0.09	28		42.5	94.7	145.4	121.9	221.9
	0.10	30		55.0	119.9	169.4	128.9	238.0

In this study, oxygen dilution of the ethylene stream in the Santoro flame was investigated and the fields of soot temperature and volume fraction were measured by the 2C-MAE technique. When the oxygen volume fraction is increased from 0 to 30% in the fuel flow, the peak f_v in the flame increases from 9.7 to 55 ppm. Thus, this experimental configuration offers the opportunity for a quantitative evaluation of the retrieved temperature deviation that is caused when the soot self-absorption is omitted for different levels of soot loading. However, it should be reminded that beyond the omission of the soot self-absorption, an additional deviation will be experimentally obtained, as the 2C-pyrometry technique is also based on a model of local spectral absorption coefficient while the 2C-MAE technique allows for its measurement.

3.3 Performance indicators

To properly assess the performances of the soot temperature measurements by the 2C-MAE or 2C-pyrometry techniques in both parametric study and experimental assessment, the absolute error (AE) and standard deviation (SD) are evaluated following Eqs. (10) and (11), respectively:

$$\mathrm{AE} = \frac{\sum_{i=1}^{M} \left| T_{\mathrm{retrieved},i} - T'_{\mathrm{retrieved},i} \right|}{M}, \quad \text{where } f_{v,i} > 1 \text{ ppm} \tag{10}$$

$$\mathrm{SD} = \sqrt{\frac{\sum_{i=1}^{M} \left(T_{\mathrm{retrieval},i} - T'_{\mathrm{retrieved},i} \right)^2}{M}}, \quad \text{where } f_{v,i} > 1 \text{ ppm} \tag{11}$$

where $T_{\mathrm{retrieved},i}$ is the retrieved soot temperature when self-absorption is ignored and $T'_{\mathrm{retrieved},i}$ is the retrieved soot temperature as soot self-absorption is accounted. Among the M measurements (typically 9000) that the technique provides within the flame, only those associated with a local soot volume fraction f_v larger than 1 ppm are accounted for to specifically assess the effect of soot self-absorption without any influence of the technique detectivity, which depends especially on the detection spectral ranges.

Within the 2C-MAE and 2C-pyrometry experimental assessment, it is worth noting that $T'_{\mathrm{retrieved},i}$ is the same temperature field, which is obtained from the 2C-MAE technique that accounts the self-absorption.

4 Results and discussion

4.1 Influence of soot loading level

This part of the parametric study is conducted with $\lambda_1 = 645$ nm and $\lambda_2 = 785$ nm as detection spectral ranges, and for the normal temperature level. The trends reported below are very similar for the other combinations of detection spectral ranges.

Figure 2 first displays the relative reduction of the spectral emission rate integrated over the line-of-sight due to soot self-absorption for the three soot loading levels at a given height above the burner (HAB). With increasing the soot loading, the self-absorption effect is more and more significant. Furthermore, this trend is more pronounced for shorter wavelength. More quantitatively, for the three soot loading levels investigated, the self-absorption causes 11%, 19%, and 39% intensity drops, respectively, in the near-infrared (785 nm) spectral range, while these reductions are 13%, 23%, and 45%, respectively, in the red spectral range.

The retrieved temperature profiles at three different heights above the burner (HAB) are contrasted with the original ones in Fig. 3. At HAB = 60 mm, when soot self-absorption is accounted for, the soot temperature profile is decently retrieved. In contrast, when the self-absorption is ignored, the higher the soot loading level, the larger is the temperature deviation. The deviation is more pronounced

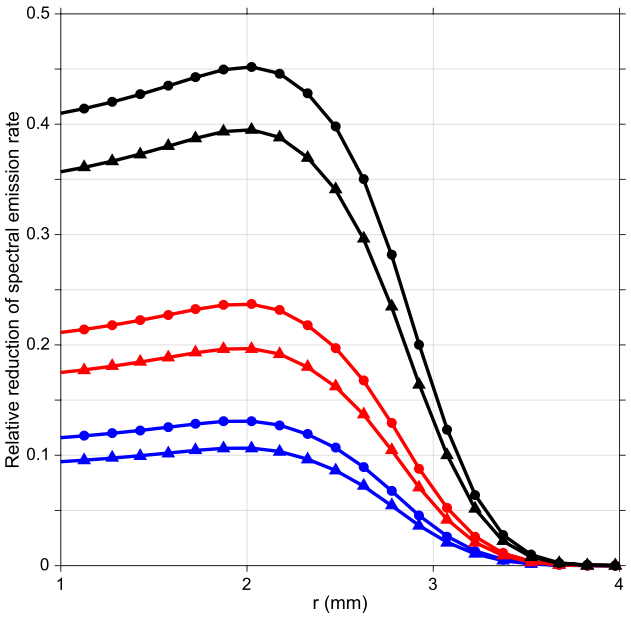

Fig. 2 Relative reduction of the computed spectral emission rate due to soot self-absorption at HAB = 30 mm as a function of the distance from the flame's axis. Circle (O) and triangle (△): reductions at $\lambda = 645$ nm and 785 nm, respectively. Blue, red, and black solid lines: low, medium, and high soot loading levels, respectively

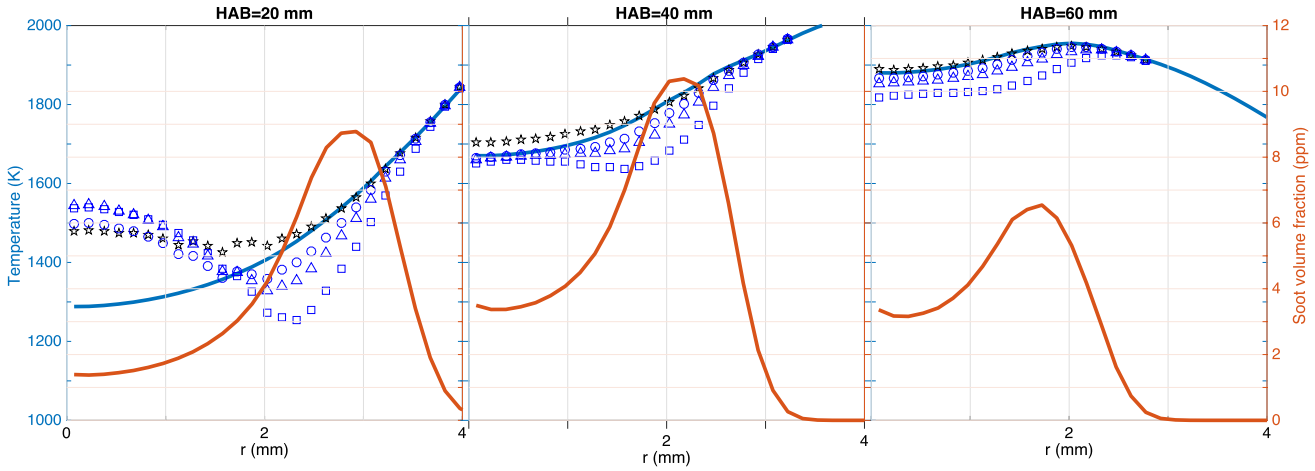

Fig. 3 Retrieved temperature profiles for different soot loading levels at three different HABs. The blue and orange solid lines are the original profiles of soot temperature (left y-axis) and volume fraction (right y-axis), respectively. The stars (⋆) indicate the retrieved temperature profiles as soot self-absorption is accounted for. The circles (O), triangles (△), and squares (□) indicate the retrieved temperature profiles as soot self-absorption is omitted for normal, medium, and high soot loading levels, respectively

in the vicinity of the axis. This is due to non-uniform self-absorption along the line-of-sight. In the central region, the soot emission experiences a higher self-absorption as compared to that outcoming emission from the outer annular region.

At HAB = 40 mm, due to the ill-conditioned deconvolution process, the retrieved temperature in the central region tends to be overestimated, which compensates the underestimation due to soot self-absorption. The temperature deviation in the annular region is similar to that at HAB = 60 mm.

At HAB = 20 mm, the soot volume fraction in the central is low and experiences a strong annular structure [32]. As a result, the temperature is more overestimated in the central region, while the underestimation in the outer region is still due to the self-absorption effect. For the higher soot loading level, the maximum temperature deviation at HAB = 20 mm (200 K) is twofold at HAB = 60 mm (100 K), which indicates that the regularization tool is required to dump the error propagation along the deconvolution process when both high soot loading level and ill-conditioning are met.

The retrieved temperature deviation due to the soot self-absorption omission is quantified by the statistical AE and SD over the whole fields for the three soot loading levels. The results are reported in Table 2.

Table 2 Retrieved temperature absolute error (AE) and standard deviation (SD) at different soot loading levels and detection spectral ranges as the self-absorption is neglected (only the locations where $f_v > 1$ ppm contributes to AE and SD)

Selected wavelengths (nm)	Conditions	AE (K)	SD (K)
$\lambda_1 = 645$			
$\lambda_2 = 485$	Soot loading		
	Normal	124.9	479.1
	Medium	215.7	683.9
	High	354.9	895.7
$\lambda_2 = 532$	Soot loading		
	Normal	50.4	86.8
	Medium	64.1	100.1
	High	65.6	342.6
$\lambda_2 = 785$	Soot loading		
	Normal	**29.3**	**44.8**
	Medium	**42.7**	**61.1**
	High	**80.3**	**139.0**

4.2 Influence of the detection spectral ranges

As mentioned previously, three couples of spectral ranges for temperature retrieval are investigated in this study. These are 645 & 485 nm, 645 & 532 nm, and 645 & 785 nm, the latest one being used in the above parametric studies. Every spectral range has been determined provided the availability of a commercial CW laser as this needs to be incorporated to the optical setup.

These couples of spectral ranges are now sequentially selected to conduct a systematic parametric study at the different soot loading levels. A selection of the subsequent retrieved temperature profiles at HAB = 20 mm is shown in Fig. 4, for (a) high soot loading level and (b) normal soot loading level. For both sets of conditions, the combination of the spectral ranges centered at 645 nm and 785 nm provides the minimum temperature discrepancy when the self-absorption is ignored. Again, the comparison between subplot (a) and (b) implies that the higher soot loading level

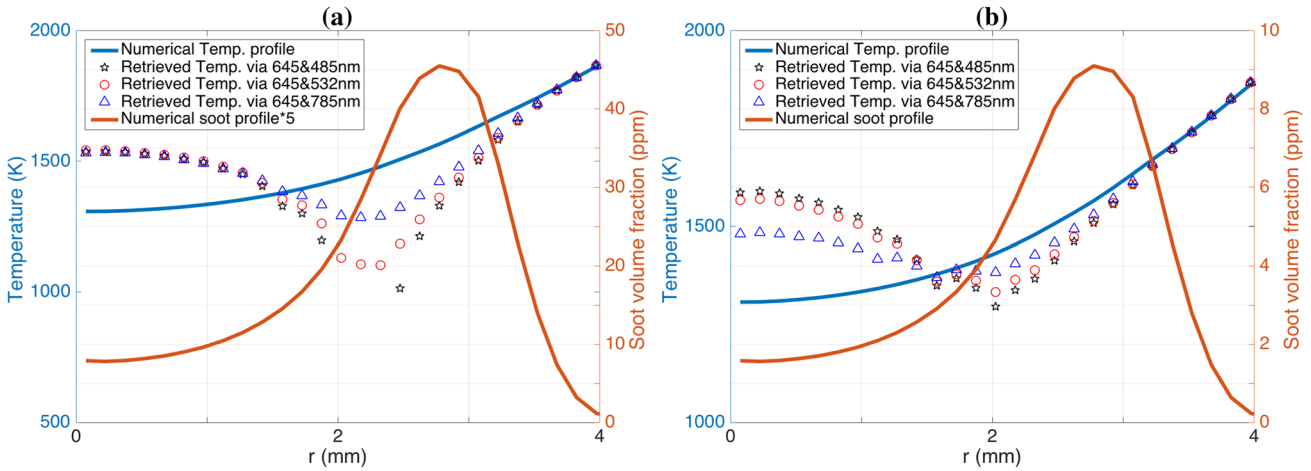

Fig. 4 Retrieved temperature profiles at HAB = 20 mm for different detection spectral ranges: **a** at high soot loading level ; **b** at normal soot loading level. The blue and orange solid lines are the original profiles of soot temperature (left *y*-axis) and volume fraction (right *y*-axis), respectively. The symbols indicate the temperature profiles that are retrieved when the self-absorption is ignored

is, the larger temperature reconstruction error caused by the omission of the self-absorption.

The evaluated AE and SD over the whole temperature fields are also reported in the Table 2. It clearly reveals that the combination of 645 and 785 nm spectral ranges leads to the most accurate temperature measurement no matter how much the soot loads in the flames.

4.3 Experimental assessment

When conducting measurements by the 2C-MAE technique, the soot self-absorption has no biasing influence on the soot volume fraction retrieval as this measurement is based on the absorption phenomenon. In contrast, the soot self-absorption does affect the temperature reconstructions. In the experimental highly sooting flames specified in Sect. 3.2, the soot self-absorption of the flame emission is expected to induce a significant retrieved temperature underestimation due to higher levels of soot absorption coefficient. Following the 2C-MAE post-processing prescribed in Sect. 2.1, both with and without including the self-absorption, AE and SD are calculated to quantitatively assess the self-absorption generated temperature discrepancies. The results are reported in the 2C-MAE columns in Table 1. Meanwhile, following the 2C-pyrometry methodology prescribed in Sect. 2.2, the additional temperature deviations attributed to the 2C-pyrometry are shown in the 2C-pyrometry columns in Table 1. As a result, Fig. 5 displays the comparisons of AE and SD variations with maximum f_v both from the experimental results (in Table 1) and numerical studies

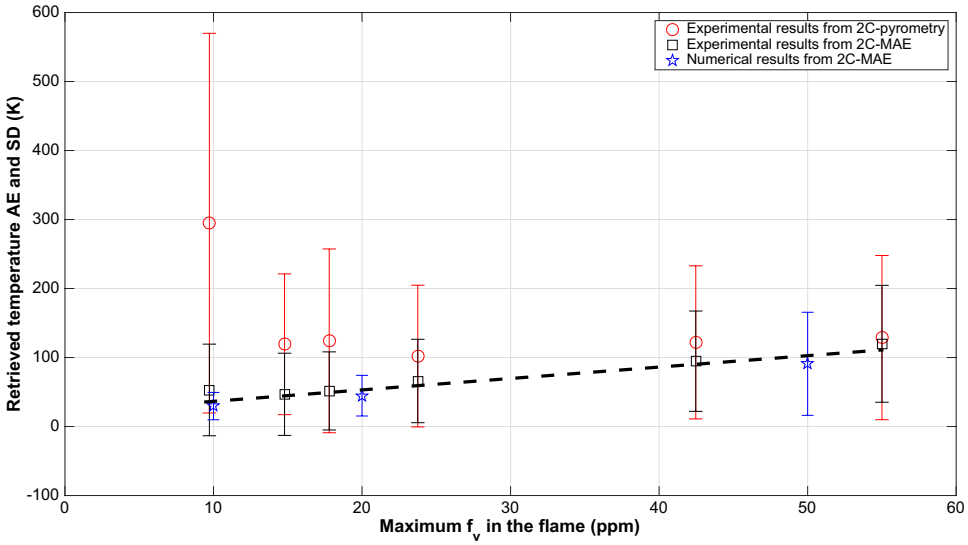

Fig. 5 Comparison of experimental and numerical retrieved temperature absolute error (AE) and standard deviation (SD) at different soot loadings (Only the locations where $f_v > 1$ ppm are calculated).The error bars represent the SD corresponding to the AE. The numerical results are obtained from Table 2, while the experimental results are processed from the oxygen-diluted Santoro flame investigations in Ref. [11], as shown in Table 1

(highlighted in bold characters in Table 2). It has to be reminded that these results are obtained with the 645 and 785 nm spectral ranges combination.

Both experimental and numerical studies of 2C-MAE fit the same linear correlation, which quantitatively indicates that the self-absorption omission causes a temperature underestimation of approximately 120 K when the maximum soot volume fraction within the flame reaches 50 ppm. Therefore, when soot volume fraction is more than 50 ppm in the flame, the emission signal trapped by the soot over the line-of-sight is required to be accounted for and corrected to achieve acceptable temperature uncertainties with the 2C-MAE technique. Provided the self-absorption is ignored, 2C-MAE generally offers more accurate temperature measurements than the 2C-pyrometry, though the temperature deviation due to the self-absorption in 2C-pyrometry technique globally decreases with increasing soot loading level.

5 Conclusion

Following the 2C-MAE procedure that intrinsically includes the soot self-absorption within the signal processing, the soot self-absorption influence on the accuracy of the retrieved temperature field could be originally quantified here as a function of the soot loading level and the combination of detection spectral ranges. In general, the relative flame emission reduction due to the self-absorption is directly proportional to the soot volume fraction and is unaffected by the temperature range. Meanwhile, the shorter wavelength of emission is more prone to be absorbed by the soot particles in the flame.

Provided the self-absorption is ignored, the higher the peak soot volume fraction within the flame, the larger is the underestimation of the retrieved soot temperature. However, when the soot volume fraction profile experiences large undulation, e.g., at HAB = 20 mm in the Santoro flame, the retrieved temperature tends to be overestimated in the central region of the flame due to the ill-conditioning of the deconvolution. Furthermore, based on the two-dimensional temperature fields, the linear correlation between the absolute error and the rising maximum f_v in the flame are quantitatively assessed by both the numerical and experimental results. It especially delineates the unacceptable temperature error boundaries in terms of maximum f_v in the flame when the self-absorption is neglected during the 2C-MAE technique implementation.

Eventually, compared to other two combinations, the combination of detection spectral ranges centered at 645 nm and 785 nm offers a weak temperature deviation, i.e., minimizes the effect of the self-absorption omission at any conditions of soot loading level.

Acknowledgements This work was supported by the Natural National Science Foundation (NSFC) (51706140). Thanks for Mr. Jérôme Bonnety for his experimental assisting.

Appendix A

Influence of soot temperature range

This part of the parametric study is conducted with $\lambda_1 = 645$ nm and $\lambda_2 = 785$ nm as detection spectral ranges and for the normal soot loading level. As the temperature elevation is increased by a factor of 1.5 and 2 to create the medium and high temperature range levels, respectively, the corresponding maximum temperature reaches approximately 3000K and 4000 K.

The relative reductions of the spectral emission rate due to the soot self-absorption at three temperature ranges are displayed in Fig.6. While the local spectral emission rate is significantly increased as temperature is elevated, the relative part of the spectral emission rate that is accumulated along the line-of-sight and transmitted to the sensor is not affected. As a result, the profiles only differ due to their spectral dependence, with peaks of 13% and 11% for 645 nm and 785 nm, respectively. Again, the shorter the wavelength, the larger is the self-absorption effect, which is consistent with the findings by Liu et al. [32].

Furthermore, retrieved temperature profiles at three different HABs are compared with the original ones in Fig. 7. When the self-absorption is neglected, the retrieved temperature underestimation tendency is the same as that shown

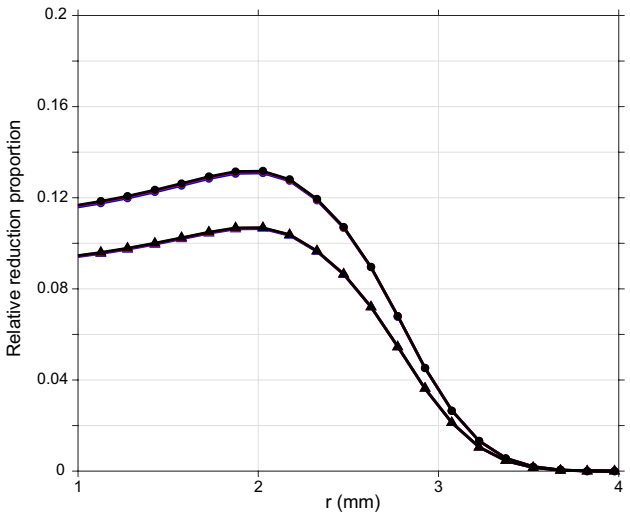

Fig. 6 Relative reduction of the computed spectral emission rate due to soot self-absorption at $HAB = 30mm$ as a function of the distance from the flame's axis. Circle (O) and triangle (△): reductions at $\lambda = 645$ nm and 785 nm, respectively. Blue, red, and black solid lines: normal, medium, and high temperature ranges, respectively

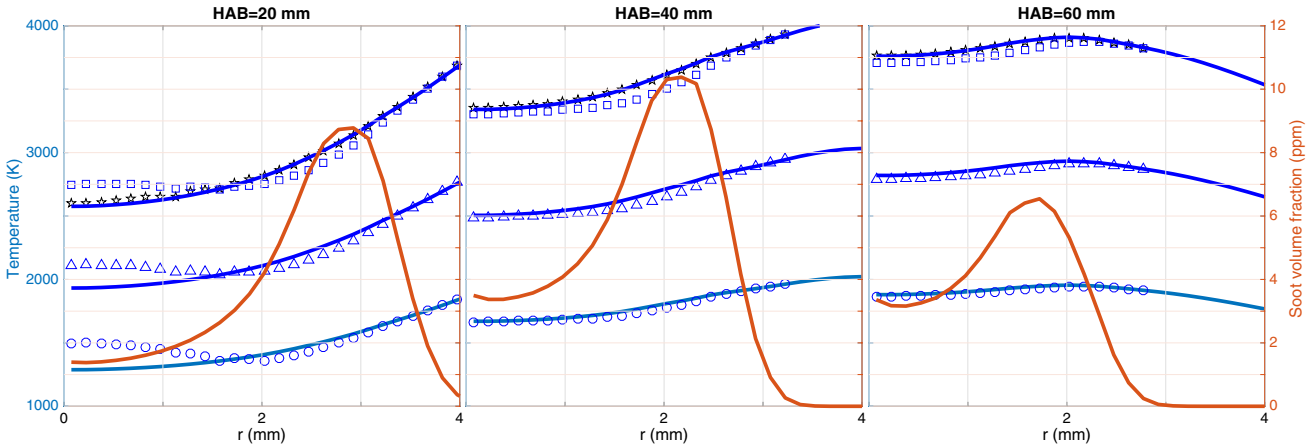

Fig. 7 Retrieved temperature profiles for different temperature ranges at three different HABs. The blue and orange solid lines are the original profiles of soot temperature (left *y*-axis) and volume fraction (right *y*-axis), respectively. The stars (⋆) indicate the retrieved temperature profiles as soot self-absorption is accounted for. The circles (O), triangles (△), and squares (□) indicate the retrieved temperature profiles as soot self-absorption is omitted for normal, medium, and high temperature ranges, respectively

for the different soot loading levels, while the temperature overestimation at the central region at HAB = 20 mm is attributed to the ill-conditioning of the deconvolution. In general, with increasing the temperature range, the temperature underestimation due to the self-absorption omission is almost the same level. These results verify that the self-absorption influence is independence of soot temperature.

References

1. M. Frenklach, H. Wang, Detailed modeling of soot particle nucleation and growth. Proc. Combust. Inst. **23**, 1559–1566 (1991)
2. I.M. Kennedy, C. Yam, D.C. Rapp, R.J. Santoro, Modeling and measurements of soot and species in a laminar diffusion flame. Combust. Flame **107**, 368–382 (1996)
3. G. Blanquart, H. Pitsch, Analyzing the effects of temperature on soot formation with a joint volume-surface-hydrogen model. Combust. Flame **156**, 1614–1626 (2009)
4. A. Khosousi, F. Liu, S.B. Dworkin, N.A. Eaves, M.J. Thomson, Experimental and numerical study of soot formation in laminar coflow diffusion flames of gasoline/ethanol blends. Combust. Flame **162**, 3925–3933 (2015)
5. C. Eberle, P. Gerlinger, M. Aigner, A sectional PAH model with reversible PAH chemistry for CFD soot simulations. Combust. Flame **179**, 63–73 (2017)
6. F. Liu, H. Guo, G.J. Smallwood, Ö.L. Gülder, Effects of gas and soot radiation on soot formation in a coflow laminar ethylene diffusion flame. J. Quant. Spectrosc. Radiat. Transf. **73**, 409–421 (2002)
7. P. Chatterjee, J. L. de Ris, Y. Wang, S. B. Dorofeev, A model for soot radiation in buoyant diffusion flame, Proc. Combust. Inst. **2**, 2665-2671 (2011)
8. R.J. Santoro, T.T. Yeh, J.J. Horvath, H.G. Semerjian, The transport and growth of soot particles in laminar diffusion flames. Combust. Sci. Technol. **53**, 89–115 (1987)
9. P.B. Kuhn, B. Ma, B.C. Connelly, M.D. Smooke, M.B. Long, Soot and Thin-filament Pyrometry Using a Color Digital Camera. Proc. Combust. Inst. **33**, 743–750 (2011)
10. Q. Wang, G. Legros, J. Bonnety, C. Morin, Experimental characterization of the different nitrogen dilution effects on soot formation in ethylene diffusion flames. Proc. Combust. Inst. **36**, 3227–3235 (2017)
11. Q. Wang, G. Legros, J. Bonnety, C. Morin, A. Matynia, J.L. Consalvi, F.S. Liu, Experimental assessment of the sudden-reversal of the oxygen dilution effect on soot production in coflow ethylene flames. Combust. Flame **183**, 242–252 (2017)
12. T. Blacha, M.D. Domenico, P. Gerlinger, M. Aigner, Soot predictions in premixed and non-premixed laminar flames using a sectional approach for PAHs and soot. Combust. Flame **159**, 181–193 (2012)
13. S. De Iuliis, F. Migliorini, F. Cignoli, G. Zizak, Peak soot temperature in laser-induced incandescence measurements. Appl. Phys. B **83**, 397–402 (2006)
14. M. Charwath, R. Suntz, H. Bockhorn, Influence of the temporal response of the detection system on time-resolved laser-induced incandescence signal evolutions. Appl. Phys. B **83**, 435–442 (2006)
15. D.R. Snelling, K.A. Thomson, F. Liu, G.J. Smallwood, Comparison of LII derived soot temperature measurements with LII model predictions for soot in a laminar diffusion flame. Appl. Phys. B **96**, 657–669 (2009)
16. S. Schraml, S. Dankers, K. Bader, S. Will, A. Leipertz, Soot temperature measurements and implications for time-resolved laser-induced incandescence (TIRE-LII). Combust. Flame **120**, 439–450 (2000)
17. F. Goulay, P.E. Schrader, H.A. Michelsen, Effect of the wavelength dependence of the emissivity on inferred soot temperatures measured by spectrally resolved laser-induced incandescence. Appl. Phys. B **100**, 655–663 (2010)
18. S. De Iuliis, M. Barbini, S. Benecchi, F. Cignoli, G. Zizak, Determination of the Soot Volume Fraction in an Ethylene Diffusion Flame by Multiwavelength Analysis of Soot Radiation. Combust. Flame **115**, 253–261 (1998)
19. D.R. Snelling, K.A. Thomson, G.J. Smallwood, L.Ö. Gülder, E.J. Weckman, R.A. Fraser, Spectrally resolved measurement

of flame radiation to determine soot temperature and concentration. AIAA J. **40**, 1789–1795 (2002)
20. I. Ayranci, R. Vaillon, N. Selcuk, F. André, D. Escudié, Determination of Soot Temperature, Volume Fraction and Refractive Index From Flame Emission Spectrometry. J. Quant. Spectr. Radiat. Transfer **104**, 266–276 (2007)
21. R.J. Hall, P.A. Bonczyk, Sooting flame thermometry using emission/absorption tomography. Appl. Opt. **29**, 4590–4598 (1990)
22. T.P. Jenkins, R.K. Hanson, Soot pyrometry using modulated absorption/emission. Combust. Flame **126**, 1669–1679 (2001)
23. G. Legros, Q. Wang, J. Bonnety, M. Kashif, C. Morin, J.L. Consalvi, F.S. Liu, Simultaneous soot temperature and volume fraction measurements in axis-symmetric flames by a two-dimensional modulated absorption/emission technique. Combust. Flame **162**, 2705–2719 (2015)
24. H.A. Michelsen, Probing soot formation, chemical and physical evolution, and oxidation: A review of in situ diagnostic techniques and needs. Proc. Combust. Inst. **36**, 717–735 (2017)
25. J. Yon, R. Lemaire, E. Therssen, P. Desgroux, A. Coppalle, K.F. Ren, Examination of wavelength dependent soot optical properties of diesel and diesel/rapeseed methyl ester mixture by extinction spectra analysis and LII measurements. Appl. Phys. B **104**, 253–271 (2011)
26. M.P. Freeman, S. Katz, Determination of the Radial Distribution of Brightness in a Cylindrical Luminous Medium with Self-Absorption. J. Opt. Soc. Am. **50**, 826–830 (1960)
27. H.A. Michelsen, Laser-induced incandescence: Particulate diagnostics for combustion, atmospheric, and industrial applications. Prog. Energy Combust. Sci. **51**, 2–48 (2015)
28. M.Y. Choi, K.A. Jensen, Calibration and correction o f laser induced incandescence for soot volume fraction measurements. Combust. Flame **112**, 485–49 (1998)
29. F. Liu, K.A. Thomson, G.J. Smallwood, Numerical investigation of the effect of signal trapping on soot measurements using LII in laminar coflow diffusion flames. Appl. Phys. B **96**, 671–682 (2009)
30. K. J. Daun, K. A. Thomson, F. Liu, Investigation of Thermal Accommodation Coefficients in Time-Resolved Laser-Induced Incandescence, J. Heat Transfer **130**, 112701-1/112701-10 (2008)
31. B. Franzelli, M. Roussillo, P. Scouflaire, J. Bonnety, R. Jalain, T. Dormieux, S. Candel, G. Legros, Multi-diagnostic soot measurements in a laminar diffusion flame to assess the ISF database consistency. Proc. Combust. Inst. **37**, (2018). https://doi.org/10.1016/j.proci.2018.05.062
32. F. Liu, K.A. Thomson, G.J. Smallwood, Soot temperature and volume fraction retrieval from spectrally resolved flame emission measurement in laminar axisymmetric coflow diffusion flames: Effect of self-absorption. Combust. Flame **160**, 1693–1705 (2013)
33. N.J. Kempema, M.B. Long, Effect of soot self-absorption on color-ratio pyrometry in laminar coflow diffusion flames. Opt. Lett. **43**, 1103–1106 (2018)
34. K.J. Daun, K.A. Thomson, F. Liu, G.J. Smallwood, Deconvolution of axisymmetric flame properties using Tikhonov regularization. Appl. Opt. **45**, 4638–4646 (2006)
35. C.F. Bohren, D.R. Huffman, *Absorption and Scattering of Light by Small Particles* (Wiley, 1983)
36. F. Cignoli, S.D. Luliis, Two dimensional two wavelength emission technique for soot diagnostics. Appl. Opt. **40**, 5370–5378 (2001)
37. H. Chang, T.T. Charalampopoulos, Determination of the Wavelength Dependence of Refractive indices of Flame Soot. Proc. Roy. Soc. Lond. A **430**, 577–591 (1990)
38. R.J. Santoro, H.G. Semerjian, R.A. Dobbins, Soot particle measurements in diffusion flames. Combust. Flame **51**, 202–218 (1983)
39. H.A. Michelsen, P.E. Schrader, F. Goulay, Wavelength and temperature dependences of the absorption and scattering cross sections of soot. Carbon **8**, 2175–2191 (2010)